We are IntechOpen, the world's leading publisher of Open Access books Built by scientists, for scientists

6,900
Open access books available

185,000
International authors and editors

200M
Downloads

Our authors are among the

154
Countries delivered to

TOP 1%
most cited scientists

12.2%
Contributors from top 500 universities



WEB OF SCIENCE™

Selection of our books indexed in the Book Citation Index in Web of Science™ Core Collection (BKCI)

Interested in publishing with us?
Contact book.department@intechopen.com

Numbers displayed above are based on latest data collected.
For more information visit www.intechopen.com



Chapter 9

Vanadium Pentoxide (V_2O_5) Electrode for Aqueous Energy Storage: Understand Ionic Transport using Electrochemical, X-Ray, and Computational Tools

Daniel S. Charles and Xiaowei Teng

Additional information is available at the end of the chapter

http://dx.doi.org/10.5772/62759

Abstract

In this book chapter, we have discussed the recent results on vanadium oxide-based materials for energy storage applications. Primarily, we present the new results from our own research group on V_2O_5-layered nanostructures that are made from a facile wet chemistry synthesis. By fine control of the synthetic condition, the morphology, crystallinity, and layer-to-layer distance of V_2O_5 nanostructures can be tuned. Particularly, highly disordered V_2O_5 nanolayers which have an interplanar distance up to 1.1 nm, offering a fast transport of K-ion between layers in an aqueous electrolyte and hence the high-energy storage capacity and power density. Uniqueness of our results includes materials characterization and measurements using multiple spectroscopic tools, including synchrotron X-ray pair distribution function (PDF) analyses and in situ X-ray diffraction (XRD). Combined with half-cell and button-cell electrochemical measurements, the complementary results provide insight on the ionic transport of ions between the layers of V_2O_5 nanostructure.

Keywords: Vanadium pentoxide, Electrochemical energy storage, X-ray diffraction, Pair distribution function, *in situ* XRD

INTECH
open science | open minds

© 2016 The Author(s). Licensee InTech. This chapter is distributed under the terms of the Creative Commons Attribution License (http://creativecommons.org/licenses/by/3.0), which permits unrestricted use, distribution, and reproduction in any medium, provided the original work is properly cited. CC BY

1. Introduction

1.1. Electrochemical energy storage

Rising demands for energy coupled with concerns over environmental pollution and dependency on petroleum fuel have contributed to a great need for new energy conversion and storage technologies [1, 2]. According to the United States Vehicle Technologies Office (VTO) at the Office of Energy Efficiency and Renewable Energy (EERE) within the Department of Energy (DOE), transitioning to a light-duty fleet of hybrid electric vehicles and plug-in electric could reduce US foreign oil dependence by 30–60% and greenhouse gas emissions by 30–45%. Thus, two approaches, both involving electrochemical processes, are generally suggested for solving this energy dilemma for the United States: (i) Development of highly efficient electrochemical energy conversion devices, such as fuel cells, as an alternative to the internal combustion engine. Such devices can use gas or liquid fuels rather than gasoline to reduce CO_2 emissions; (ii) Development of highly efficient electrochemical energy storage (EES) devices, such as Li-, Na-, or K-ion batteries, and electrochemical capacitors, to accelerate the adoption of electrical vehicle and renewable non-carbon-emitting energy from solar and wind energy sources [3, 4].

Technology	Lithium-ion battery	Electrostatic capacitor	Electrochemical capacitor
Installation cost ($/kWh)	200–360	300–2000	9000
Installation cost ($/kW)	1000	100–300	300
Energy density (Wh/kg)	160	0.01–0.1	1–10
Power density (W/kg)	180	10^4–10^7	10–10^5
Cycle life	~10^3 cycles	>15 years	10^6 cycles

Table 1. Properties of different electrical energy storage devices.

Many EES devices, including most batteries and the majority of electrochemical capacitors,

$$MO_X + A^+ + e^- \leftrightarrow MO_XA \quad (1)$$

where MO_X is a transition metal oxide, and A^+ denotes the alkali ions (e.g., Li^+, Na^+ or K^+). Upon the insertion or de-insertion of A^+, metal (M) cations will be reduced or oxidized to balance the charge. When an EES device is charged, a voltage (V) will build up between the anode and the cathode. The energy density (E) depends on the capacitance (C) and voltage of the device, while the power density (P) depends on the voltage and equivalent internal resistance (R_S) of the device, as following equations show:

$$E = \tfrac{1}{2} C V^2 \quad (2)$$

http://dx.doi.org/10.5772/62759

$$P = V^2 / (4R_S) \quad (3)$$

To provide clean and efficient energy solutions, a new genre of EES devices that are able to fill the gap between high-energy-density battery devices and high-power-density electrostatic capacitor devices are in great demand. From Eqs. (2) and (3), it is clear that to increase energy density and power density of EES devices, one needs to:

- Synthesize nanostructured electrodes that possess tailored, high-surface-area architecture that offers more redox-active sites for electrolyte and accelerated ion conductance (to increase C and decrease R_S, and hence increase E and P);
- Modify the electrode materials by adding secondary elements which could bring new functionalities for storing multiple charges at a single site of the metal oxides nanostructure (to increase C, and hence E) and could also contribute to highly reversible charge storage for better stability;
- Discover new types of charge carrier (such as bi- and/or tri-valent cations) that may increase charge storage capacity for the same amount of ionic transport (to increase C and hence E).

1.2. Current state of knowledge of Na-ion-based aqueous EES

Current EES can be classified into aqueous and non-aqueous storage according to the chemistry of the electrolytes. Non-aqueous electrolytes can achieve wider voltage window (usually >3.0 V), and thus, non-aqueous EES usually exhibits much higher-energy density than aqueous counterparts. However, non-aqueous systems are expensive and often require the use of highly toxic and flammable solvents, which can become hazardous if used improperly, such as overcharging or short-circuiting. Non-aqueous EES devices, including lithium ion batteries (LIBs), require strict preparation standards at high cost, to allow for water- and oxygen-free cell fabrication. On the other hand, aqueous EES has narrow voltage window, typically around 1.2 V, limited by oxygen and hydrogen evolution reactions of water. However, aqueous electrolytes are generally inexpensive. Water- and oxygen-fee manufacturing environment (lower than 2 ppm [part per million]) required by non-aqueous EES is unnecessary for aqueous EES, which lowers the cost of cell packing dramatically. Also, aqueous EES can use electrolytes with high salt concentration and hence have nearly two orders of magnitude higher ion conductivities compared to non-aqueous electrolytes. Aqueous lead acid batteries (LABs) are one of the most commonly used aqueous EES devices and have great advantages such as low cost and high surge current compared to LIBs. However, LABs have a short cycle life, and their components such as lead and sulphuric acid are not environmentally friendly. Other aqueous EES devices, especially rechargeable ones using earth-abundant and non-toxic electrode materials and Na- and/or K-ions as charge carriers, appear more appropriate for stationary energy storage to be used with renewable energy sources due to lower cost of raw material, longer cycling life, and better environmental friendliness compared to Li-ion and lead acid-based counterparts [5–7].

Na-ion- and K-ion-based aqueous energy storage devices have showed great potential as a new class of energy storage devices as alternatives to Li-ion storage devices, since the electrochemical potential of Na and K is almost identical to that of Li-ions. Although radii of the bare ions is in the order of $Li^+ < Na^+ < K^+$ (**Table 2**), due to the effect of hydration number (number of water molecules that migrate with each cation) of alkali metals, total radius of Na- and K-ion and their bound water molecules (Stokes radius) actually are smaller in the order of $K^+ < Na^+ < Li^+$, resulting in a higher chemical diffusion coefficient of Na- and K-ions in the aqueous electrolyte compared with Li-ions. Moreover, current mineable Li resources can be sustained for approximately only 65 years at most. In contrast, Na and K are about 1,000 times more abundant in earth crust and hence more economical. Thus, aqueous energy storage devices based on Na- and K-ions holds great promise for economical and sustainable energy storage devices with high stability, better ionic conductivity, and low cost. In this context, to find a suitable electrode materials and architecture, which guarantees a reversible intercalation and deintercalation of Na- and K-ions, while maintaining a stable electrode and electrolyte interface, becomes imperative to the design of new generation of energy storage devices.

	Ionic conductivity in water (/10^{-4} Ω^{-1} m^2)	Atomic radius (/pm)	Ionic radius (/pm)	Hydration number
Li	38.7	152	60	14
Na	50.1	186	95	8.4
K	73.5	227	133	5.4

Table 2. Radii and ionic conductivities of various alkali metals in water at 298 K.

1.3. Layered vanadium oxides nanomaterials for EES

Charge storage mechanisms involving intercalation and deintercalation of alkaline ions has been commonly found in ESS devices with a high-energy density, such as batteries. Although intercalation process is highly reversible and suitable for the high capacity energy storage, intercalation materials usually are not suitable for high rate performance. This is largely due to the fact that the diffusion of intercalated ions (e.g., alkaline ions) in the electrode materials is sluggish, having diffusion coefficients in the range from 10^{-13} to 10^{-17} m^2/s. To shorten the diffusion time (τ), that is the time required for alkaline ions move through the host electrode material, one has to either reduce the ionic path of alkaline ions within the electrode material (L) or increase the diffusion coefficient of alkaline ions in the solid phase (D) [8], described by the following equation:

$$\tau = L^2 / D \tag{4}$$

Since the diffusion coefficient (D) is one of the intrinsic properties of alkaline ion-host electrode material couple, the only practical way to decrease the diffusion time (τ), and hence increase the rate performance of the electrode material, is to decrease the diffusion length. In this context, diffusion time can be considered as the minimum time required by the alkaline ions

http://dx.doi.org/10.5772/62759

to insert and become homogenously distributed within the host electrode material. Hence, a diffusion time of alkaline ions within host solid electrode is closely related to the C-rate of an EES device, which is a measure of the rate at which an EES device is discharged relative to its maximum capacity (1/n C-rate means that the discharge current will discharge the entire device in n hours).

τ (s)	C-rate	L^2 (nm^2)	L (nm)
36,000	0.1	360,000	600
3600	1	36,000	190
360	10	3600	60
36	100	360	19
10	360	100	10

Table 3. Relationship between the diffusion time (τ), C-rate, and diffusion length (L) of transport of alkaline ions within the electrode materials.

Table 3 describes relationship between the diffusion time (τ), C-rate, and diffusion length (L), assuming the diffusion coefficient of alkaline ions within metal oxide electrode materials is in the order of 10^{-17} m^2/s. Considering 36,000 s (10 h) a reasonable time to completely charge and discharge a battery device, a maximum diffusion length of 600 nm is needed. And this value appears to be easily achieved through tailoring the conventional preparation routine for the electrode materials. However, for a high-rate EES device that affords charge and discharge time around 36 s, a much shorter diffusion length of 19 nm is required, which might be too small to be prepared via conventional preparation routine, which typically involves a solid state reaction through decomposition of carbonate salts at high temperature (usually >500°C). A more likely prospective method to prepare nanoscaled electrode materials for shorter diffusion time is the synthesis of layered electrode structure. Many dioxides of transition metals consist of [MO_6] (M: Mn, Ti, V, Ir, Ru, Cr) octahedra with shared vertices and edges. Stacking of [MO_6] octahedra enables the building of two-dimensional layered structures [9–14]. Water molecules and alkaline ions such as Li^+, Na^+, or K^+ can easily move into or out of the layers without significant structural rearrangements. Particularly, large interplanar distance (usually close to 1 nm) favors the storage of alkaline cations and a higher capacitance [15].

Among various transition metal oxides, vanadium pentoxide (V_2O_5) has attracted great interest in the fields of electrochromic devices and as electrode materials for batteries and electrochemical capacitors, thanks to its low cost and ability to exist in different oxidation states from V^{2+} to V^{5+}. Layered vanadium oxides structures have been synthesized using electrodeposition, deposition under ultra-high-vacuum conditions or a top-down solution-phase synthesis [16, 17]. Particularly, solution-phase exfoliation methods that can synthesize layered nanostructures in large quantities have been well studied. High-temperature pre-treatment was usually required, and intercalators (e.g., tetrabutylammonium ions) were used to assist the separation of layers and hamper the reassembly of the bulk laminar material. Furthermore, by appropriate control of the chemical nature of the solvent, intercalators, exfoliation time, and temperature,

as well as the post-treatment temperature, it is possible to tune the dimension of the interplanar distance in order to improve the electrochemical performance, that is, to make the interlayer distance large enough to be capable of accommodating the alkaline ions and water.

2. Highly crystalline V_2O_5-layered electrode material for aqueous K-ion storage

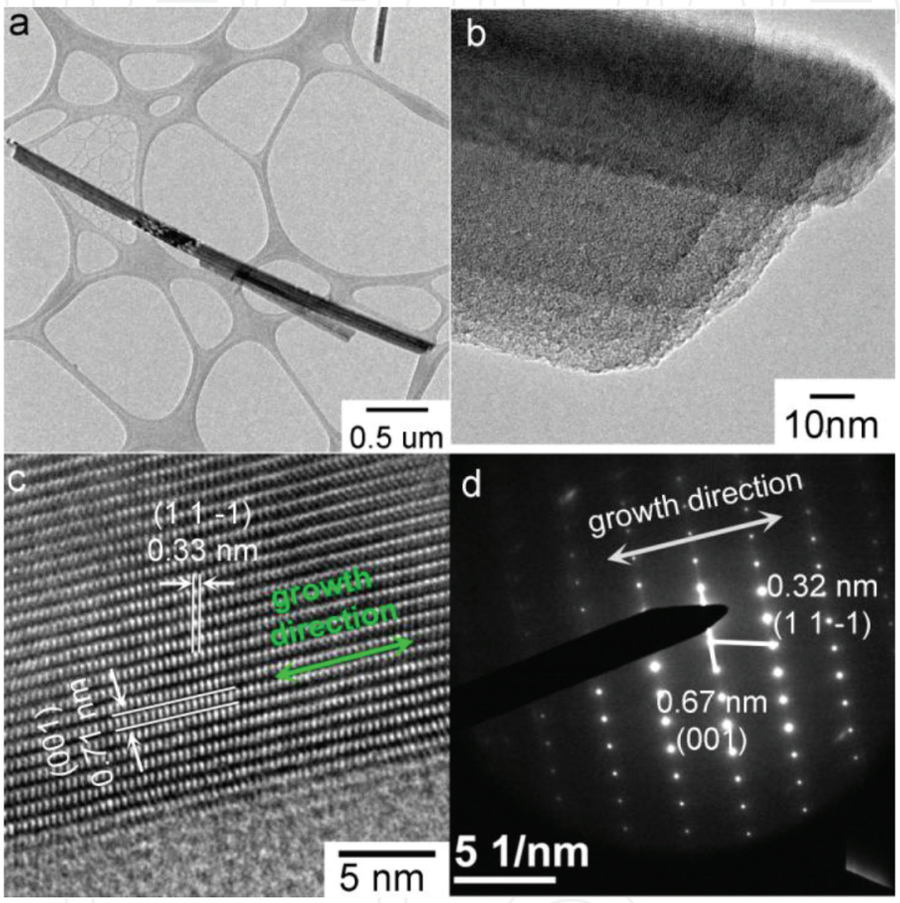


Figure 1. (a–c) TEM images of $K_{0.33}V_2O_5$-layered nanostructure after being annealed at 450°C and (d) selected-area electron diffraction of such materials.

V_2O_5-layered nanofibers can be synthesized by a facile two-step method involving solution-phase procedure followed by mild thermal treatment in the air [18]. In the first step, nearly amorphous vanadium oxides were prepared by mixing vanadyl (IV) sulfate hydrate with potassium hydroxide under vigorous stirring in water at room temperature. The resulting precipitations were dried in vacuum and then heated to 450°C for 2 hr in air. **Figure 1** shows TEM images of the final product after thermal treatment, showing a layered V_2O_5 nanofiber with an average diameter of ~120 nm and a length in a scale of micrometres. The "rolling-up" formation of the layered nanofibers is subsequently proposed based on TEM observations, suggesting that [VO_6] building units were exfoliated into layered $K_{0.33}V_2O_5$ sheets at mild temperature with intercalated K-ions within between the layers with a large interplanar

http://dx.doi.org/10.5772/62759

distance of 0.96 nm. The results suggested nanolayers rolled up along <001> direction, which appeared to be the most energetically favorable mechanism due to the large periodicity of the nanolayers.

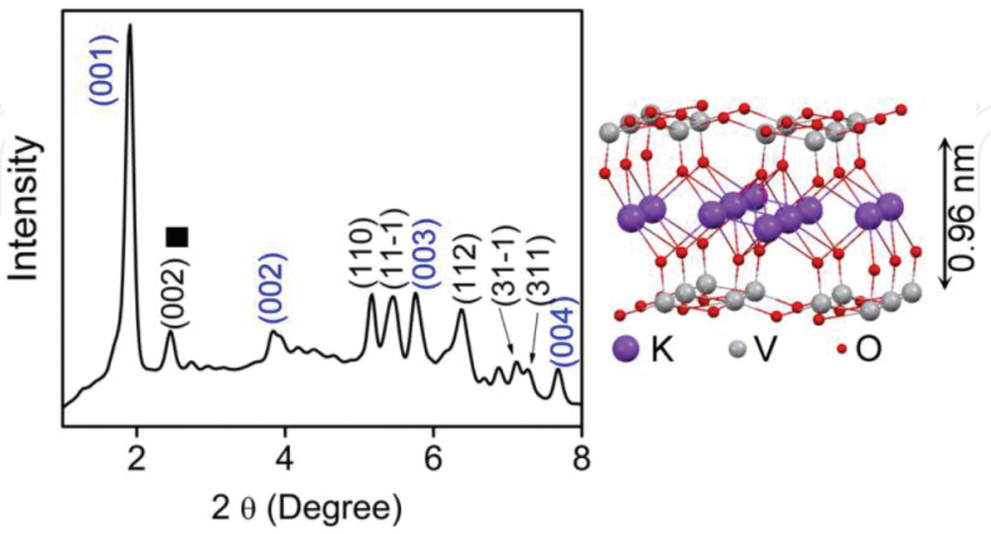


Figure 2. XRD patterns and crystalline schematics of $K_{0.33}V_2O_5$-layered nanofibers heat treated at 450°C. Wavelength of X-ray was 0.3196 nm. Diffractions from layered KxV_2O_5 (JCPDS 81045) and non-layered KxV_2O_5 (JCPDS 27718) were labeled in black and blue.

Figure 1c shows the high-resolution TEM (HRTEM) image of the final layered nanofiber with a uniform lamellar structure. An average repeating distance of 0.71 nm between the layers was observed over almost the entire layered nanofiber in the direction parallel to the longitudinal axis (growth direction). In addition to this periodic stacking of the layers, a clear fringe spacing of 0.33 nm was also observed from HRTEM imaging. **Figure 1d** shows the selected-area electron diffraction (SAED) pattern from the same layered nanofibers shown in **Figure 1c**, showing a single-crystalline nature of the layered nanofibers demonstrated by the discrete diffraction. The fringe distances were calculated from SAED to be 0.67 and 0.32 nm, matching well with the distances calculated from HRTEM. These values also matched well with d-spacing values from $K_{0.49}V_2O_5$ crystal (JCPDS 81045). The interplanar distance (d_{001} = 0.71 nm) obtained from HRTEM was smaller than that calculated from X-ray diffraction (XRD; 0.96 nm), which can be explained by the removal of structured water between the nanofibers' layers while under high vacuum and the consequent contraction of the interplanar distance of layered nanofibers during HRTEM analysis.

XRD patterns of the resulting product in which two series of reflections were shown in **Figure 2a**, which contained the conventional (hkl) set of reflection, and the (00l) set of diffraction with a high-degree ordering of the lamellar structures. The XRD reflection was in good agreement with potassium-intercalated layered V_2O_5 ($K_{0.49}V_2O_5$, JCPDS 81045), except that the peak at 2θ = 2.46° was indexed as the (002) plane of non-layered $K_XV_2O_5$ (JCPDS 27718). The strongest diffraction peak at 2θ = 1.98° was indexed to the (001) basal reflection with a corresponding d-spacing (d001) of 0.96 nm. Energy dispersive X-ray spectroscopy revealed

the chemical composition of the final product that contained 83.7% V and 13.6% K (atomic percentage) with a chemical formula of $K_{0.33}V_2O_5$.

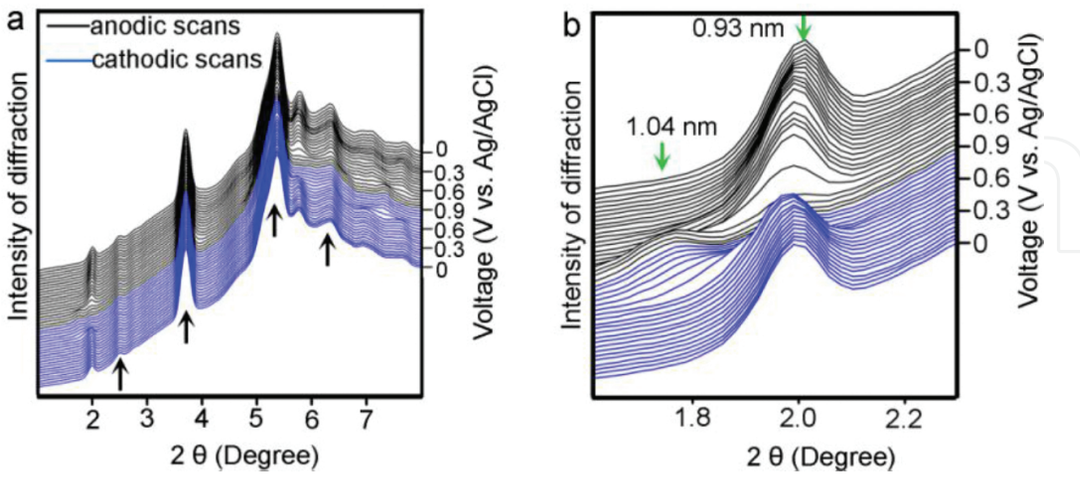


Figure 3. (a) *In situ* XRD of $K_{0.33}V_2O_5$-layered nanofibers at potentials from 0 to 0.9 V (vs. Ag/AgCl). The diffraction peaks from graphite oxide were marked by black arrows. (b) The evolution of the (001) planes upon the CV cycling.

Figure 3a shows a series of time-resolved XRD patterns of $K_{0.33}V_2O_5$-layered nanofibers using an electrochemical cell that the authors have reported in detail elsewhere. XRD patterns were obtained during anodic (black curves) and cathodic scans (blue curves) within the potential window between 0 and 0.9 V using a cyclic voltammetry (CV) program at a scan rate of 1 mV/s. Compared to the powder diffraction shown in **Figure 2**, steady diffraction background from the aqueous electrolyte solution and the commercial carbon paper from the in situ electrochemical cell were observed (marked by black arrows). The $K_{0.33}V_2O_5$-layered nanofibers showed varied peak intensities and positions at different potentials, suggesting dynamic changes of crystalline structure during the Faradaic processes, while the diffraction of layered nanofibers remained unchanged after one complete CV cycle. The results suggest that $K_{0.33}V_2O_5$-layered nanofibers possessed a reversible surface-controlled capacitive process, as well as a stable layered crystalline structure during the charge/discharge processes.

The changes of (001) diffraction peaks during the CV cycling are shown in **Figure 3b**. During the anodic scan, d-spacing of (001) plan (d_{001}) expanded from 0.93 nm ($2\theta = 1.98°$) to 1.04 nm ($2\theta = 1.76°$), corresponding to a 12% expansion of interplanar distance. On the other hand, d_{001} contracted from 1.04 to 0.95 nm during the cathodic scan. The expansion and contraction of d_{001} match very well with the charge storage mechanism of electrochemical extraction and insertion of K-ions into $K_{0.33}V_2O_5$-layered nanofibers. During the anodic scan, oxidation of $K_{0.33}V_2O_5$-layered nanofibers took place, accompanied with the removal of K-ions from interplanar layers of $K_{0.33}V_2O_5$. These processes can be expressed by the forward reaction of following equation:

$$K_{0.33}V_2O_5 \leftrightarrow K_{0.33-x}V_2O_5 + xK^+ + Xe^- \quad (5)$$

http://dx.doi.org/10.5772/62759

where x is the molar fraction of extracted K-ions. Depletion of K^+ weakened the electrostatic interaction between K-ions and negatively charged [VO_6] octahedral units within the layers, and increased the interplanar distance (d_{001}). Conversely, during the cathodic scans, $K_{0.33}V_2O_5$-layered nanofibers were reduced, accompanying with the insertion of K-ions into interplanar layers [backward reaction in Eq. (5)]. The strengthened electrostatic interaction between [VO_6] and K-ions decreased the interplanar distance.

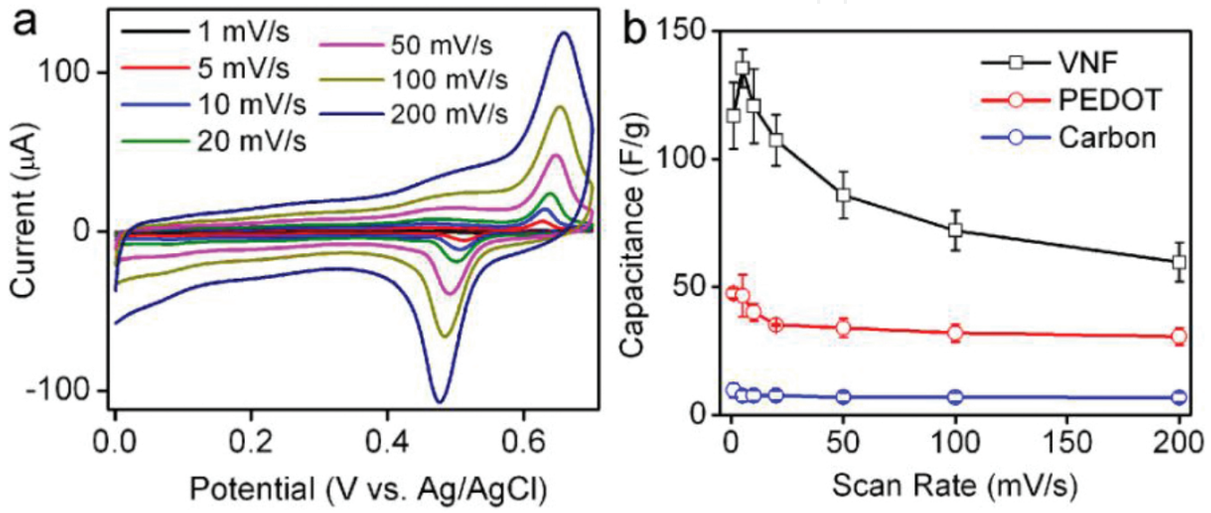


Figure 4. Three-electrode half-cell analyses: (a) CVs of $K_{0.33}V_2O_5$-layered nanofibers/PEDOT as loading of 5 and 1.25 μg, respectively; (b) gravimetric capacitance of $K_{0.33}V_2O_5$, PEDOT, and active carbon as functions of scan rates.

Figure 4a shows the cyclic voltammograms (CVs) of the mixture of $K_{0.33}V_2O_5$-layered nanofibers and PEDOT, respectively. The PEDOT and active carbon only electrodes showed broad redox peaks (data are not shown here), Indicating sluggish redox kinetics of K-ions. In contrast, the $K_{0.33}V_2O_5$/PEDOT electrode showed well-defined anodic and cathodic peaks (**Figure 4a**), representing the K^+ extraction and insertion behavior, occurring at ~0.6 (anodic scans) and ~0.5 V (cathodic scans), respectively. The calculated gravimetric capacitance (C_{MS}) was strongly dependent on the scan rate as shown in **Figure 4b**. As the scan rate decreased, C_{MS} increased. At a scan rate of 5 mV/s, the C_{MS} reached the maximum value of 136 F/g (based on $K_{0.33}V_2O_5$ mass). In general, the electrical conductivity of bulk V_2O_5 is low (10^{-5} ~ 10^{-3} Ω cm), so the addition of highly conductive PEDOT into $K_{0.33}V_2O_5$ improves the rate capability, although the C_{MS} value of the $K_{0.33}V_2O_5$/PEDOT electrode was associated strongly with the $K_{0.33}V_2O_5$ as shown in **Figure 4b**.

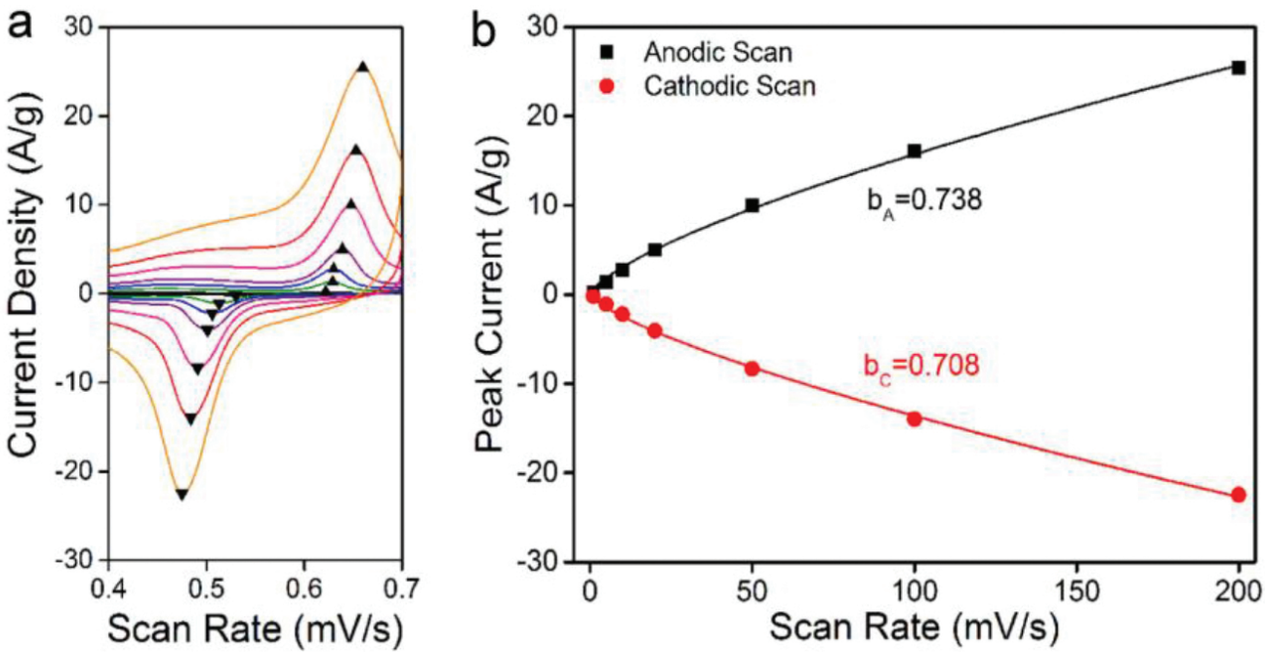


Figure 5. Calculated b-values of $K_{0.33}V_2O_5$-layered nanofibers from CV analyses at various potentials.

Charge-storage mechanism of K-ion within the $K_{0.33}V_2O_5$ electrode can be understood by analyzing current–voltage relationship provided by CV scans at different scan rates. Assuming that the peak current (i) obeyed the power law relationship with scan rate (v) at a given potential and was express as a combination of surface-controlled capacitive effects ($i_1 = k_1v$) and diffusion-controlled K-ion intercalation ($i_2 = k_2v^{½}$):

$$i = k_1v + k_2v^{½} \tag{6}$$

Accordingly, for the peak current response at a given potential can be described by a simple power law:

$$i = av^b \tag{7}$$

where a is adjustable parameter and b is equal to 0.5 or 1 when currents are strictly dominated by diffusion-controlled K-ion intercalation or surface-controlled capacitive effects. Thus, the contributions from capacitive charge and diffusion-limited redox charge during the CV cycling were extracted precisely. **Figure 5** shows typical power law regression analyses of i vs ν plot for the both anodic and cathodic CV scans with scan rates ranging from 5 to 200 mv/s. The b-value was calculated to be 0.738 during the anodic scan and to be 0.708 during cathodic scan, indicating that combination of both surface-controlled capacitive process and diffusion-limited redox process contributed significantly to the redox behavior of $K_{0.33}V_2O_5$-layered nanofibers.

http://dx.doi.org/10.5772/62759

3. Highly disordered V_2O_5-layered electrode material for aqueous K-ion storage

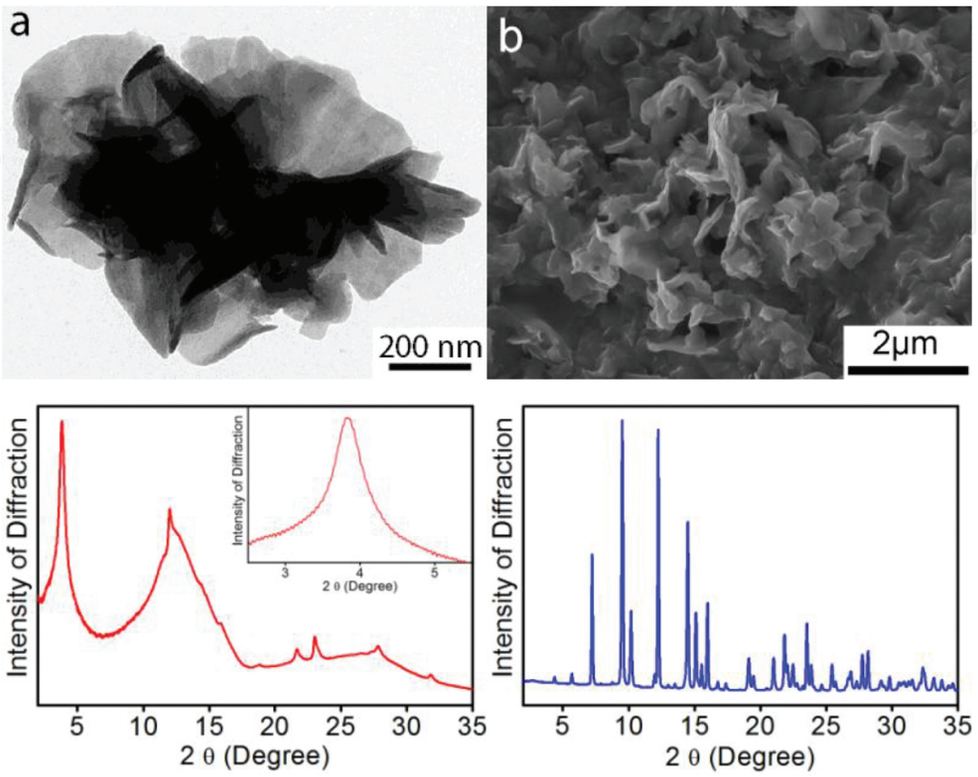


Figure 6. (a) TEM image of the $K_{0.2}V_2O_5$ nanosheets. (b) SEM image of network formed by the nanosheets. (c) X-ray diffraction (λ = 0.72768 Å) of the disordered nanosheets. (d) X-ray diffraction of bulk V_2O_5.

Disordered $K_{0.2}V_2O_5$ nanosheets were synthesized in an analogous way to the previously mentioned crystalline $K_{0.33}V_2O_5$ nanofibers, utilizing an aqueous reaction at room temperature between potassium hydroxide with vanadyl (IV) sulphate hydrate to form an amorphous VOx precursor. The amorphous VOx precursors then underwent a washing and drying process and were then thermally treated at low temperature and short time in air to form the disordered $K_{0.2}V_2O_5$ nanosheets. In **Figure 6a, b** TEM and SEM images of the disordered $K_{0.2}V_2O_5$ nanosheets are shown the sheet dimensions vary from sheet to sheet but are on the order of hundreds of nanometres. When loaded in more concentrated manner, they form a network of nanosheets. EDS measurements found that the atomistic ratio of the potassium to vanadium ratio was 9.731% K to 9.0269% V, resulting in the chemical formula of $K_{0.2}V_2O_5$.

The XRD spectra of the disordered nanosheets in **Figure 6c** contained only a few very broad peaks due to the large degree of disorder within the structure. The strong low angle peak at 3.82° 2θ was indexed as the (001) plane. The d-spacing between the layers of the disordered nanosheets is 10.916, but other structural data are hard to extract due to the severe broadening caused by the disorder. In contrast, **Figure 6d** is the XRD spectra of highly crystalline bulk V_2O_5. It contains very sharp well-defined peaks and can be easily identified as orthorhombic

structure with Pmmn symmetry and lattice parameters of a = 3.563, b = 11.50870, c = 4.375 (**Figure 7**).

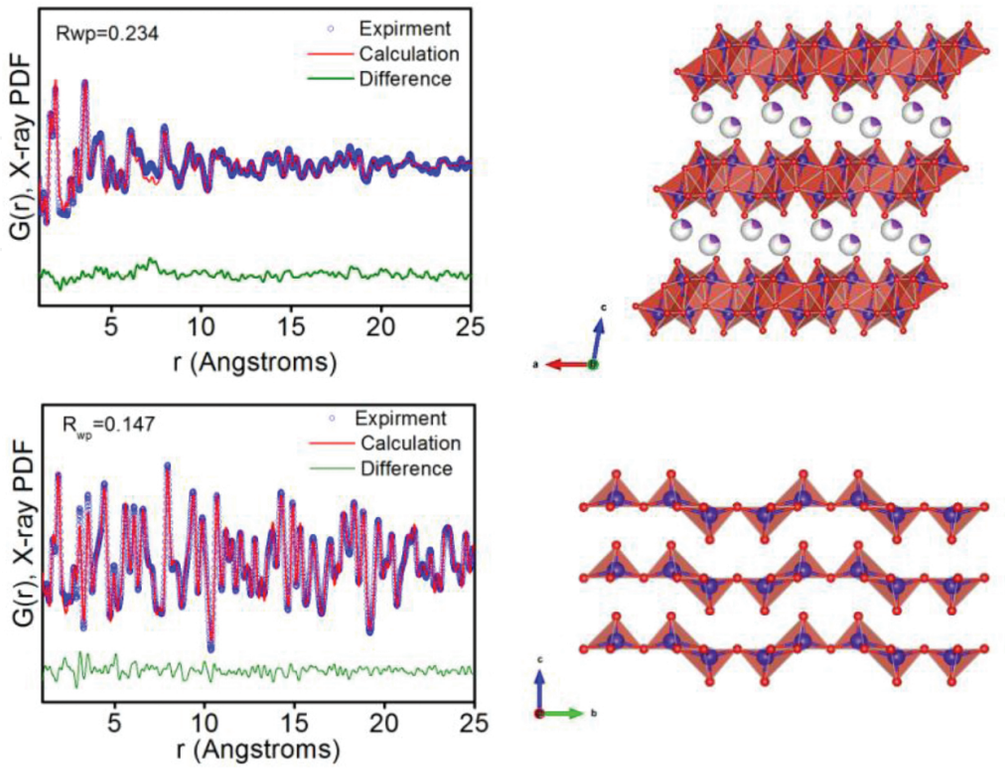


Figure 7. X-ray atomic pair distribution function analysis: (top left) disordered nanosheets and (top right) the solved crystal structure of bi-layered [VO_6] octahedral layers with a potassium intercalate. (Bottom left) bulk V_2O_5 and (bottom right) the bulk crystal structure.

Due to lack of crystallinity, there is much broadening of the peaks in the XRD spectra, and the atomistic crystal structure was not able to be accurately identified. Therefore, the local structure of the disordered nanosheets was characterized by total X-ray total scattering experiments and refinement of the atomic pair distribution function (PDF). The PDF is calculated by taking the sine Fourier transform of the total structure factor and is a real-space representation of inter atomic distances through a radial distribution function. PDF takes into account both the Bragg diffraction and diffuse scattering caused by local nonperiodic structural defects allowing for the investigation of disordered materials. Total scattering experiments can be done with both neutrons and X-rays allowing for good resolution between elements.

The major phase identified in the PDF of the disordered nanosheets was a monoclinic structure with a C2/m symmetry. It was made of V_2O_5 bilayers consisting of distorted [VO_6] octahedra and a potassium intercalate within the bilayers. The bulk orthorhombic V_2O_5 phase consisting of [VO_5] polyhedra was also detectable in the PDF of the disordered nanosheets. Based in the refinement, the sample was comprised of 72% monoclinic phase and 28% of the orthorhombic phase by weight. The short range order in the disordered nanosheets is dominated by the monoclinic phase, which is only ordered out to 14 Å, accounting for the initial sharp decrease

http://dx.doi.org/10.5772/62759

in the intensity of the PDF. The long range order is dominated by orthorhombic phase. The X-ray PDF of the bulk V_2O_5 is sharper and more intense as compared to the nanosheets due to the high crystallinity. The results of the real-space refinement of the PDF and the Rietveld refinement in reciprocal space of the XRD spectra are nearly identical.

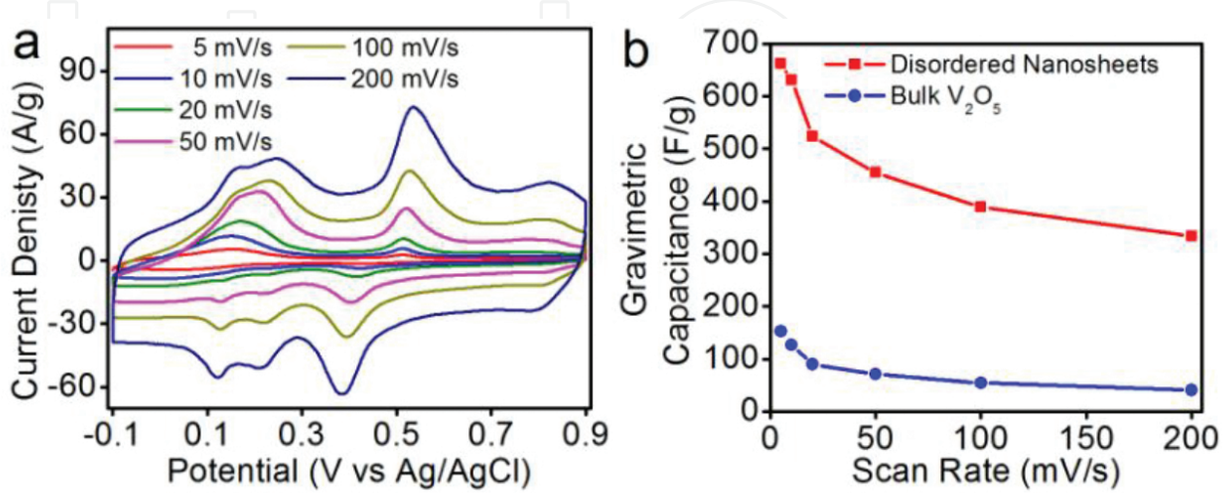


Figure 8. Three-electrode half-cell analyses: (a) CVs of $K_{0.2}V_2O_5$ disordered nanosheets/PEDOT as loading of 5 and 1.25 μg, respectively. (b) Gravimetric capacitance of $K_{0.2}V_2O_5$, bulk V_2O_5 and as a function of scan rate.

The electrochemical behavior of the layered $K_{0.2}V_2O_5$ disordered nanosheets material was investigated utilizing a three-electrode half-cell with a rotating disk electrode. Aqueous inks were made with the 4:1 ratio of disordered nanosheets material to poly (3,4-ethylenedioxy-thiophene) (PEDOT), a conductive polymer. CV measurements were conducted in a neutral aqueous 1 M KCl electrolyte solution with a 1 V potential window from −0.1 to 0.9 V versus a saturated KCl Ag/AgCl reference electrode. CV measurements at various scan rates between 5 and 200 mV/s are shown in **Figure 8a**. Three distinct oxidation peaks are observable in the anodic scan at 0.20 V, 0.53 V, and 0.78 V. The corresponding peaks of all three redox couples can be observed in the cathodic scan at 0.16 V, 0.38 V, and 0.79 V. All of the redox peaks remain visible throughout all of the scan rates tested.

The $K_{0.2}V_2O_5$ nanosheets exhibit excellent capacitance at low scan rates, 661 F/g (183 mAh/g) at a scan rate of 5 mV/s in 1 V potential window. A significant amount of capacitance was retained even at higher scan rates, and 334 F/g (93 mAh/g) at 200 mV/s. 52% of the specific capacitance was retained with a 40-times increase in scan rate, from 5 to 200 mV/s. Assuming one charge transfer per vanadium atom, the theoretical capacitance of V_2O_5 is 294 mAh/g, 0.6 electron transfer per vanadium atom. As shown in Eq. (4), the amount of potassium atoms inserted is directly proportional to the charge stored, when fully reduced at 5 mV/s the amount of potassium inserted is equivalent to $K_{1.2}V_2O_5$ and at 200 mV/s the amount of potassium inserted is equivalent to $K_{0.6}V_2O_5$.

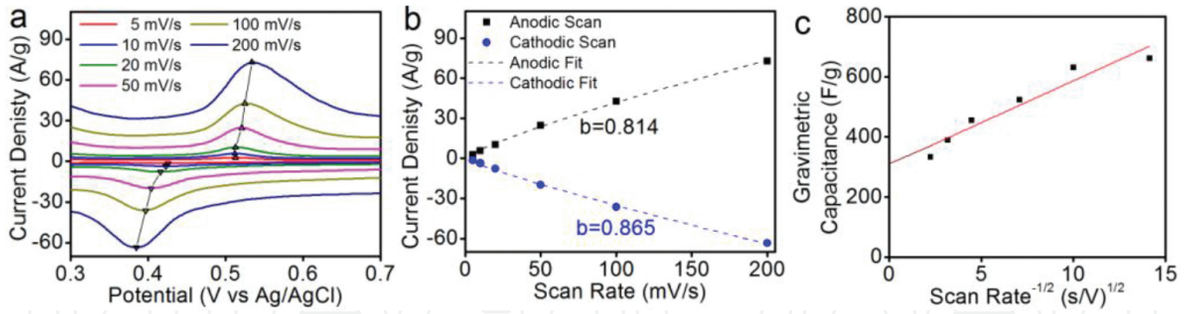


Figure 9. (a) Anodic and cathodic redox peaks from the CV measurement of the disordered $K_{0.2}V_2O_5$ nanosheets at 0.53 and 0.38 V, respectively, and (b) the corresponding b-value calculation. (c) Infinite sweep rate extrapolation.

To further investigate the charge storage mechanism, the data from CV measurements was further exploited with electrokinetic analysis. The scan rate (v) vs. peak current for the redox couple shown in **Figure 9a** was analyzed with the b-value evaluation from Eq. (6). The results of the fitting are shown in **Figure 9c**. The anodic scan had a b-value of 0.814, and the cathodic scan had a b-value of 0.865. Both processes seem to be similar in mechanism having similar b-values, with the oxidation process associated with the anodic scan being slightly more diffusion limited than the reduction process associated with the cathodic scan. As compared to the crystalline $K_{0.33}V_2O_5$ nanofibers, the b-value of the disordered nanosheets is closer to 1; evidence that the disordered nanosheets are less diffusion limited then crystalline nanofibers.

Further information can be obtained by extrapolation to an infinite scan rate. The total charge (q_T) stored can be expressed as the sum of the charge stored at the surface by capacitive charge storage process and the charge stored in the bulk by diffusion limited diffusion process. The charge stored on the surface is from capacitive processes, that is, double-layer/under potential deposition, charge separation at the surface, and pseudocapacitive reversible near-surface redox reactions and is assumed to be constant (q_∞) with varying scan rate. Semi-infinite linear diffusion is assumed for the intercalation process into the bulk and is approximated with a constant (c) multiplied by the inverse square root of scan rate ($v^{-1/2}$)

$$q_T(v) = q_\infty + cv^{-1/2} \tag{8}$$

The extrapolated specific capacitance for the disordered $K_{0.2}V_2O_5$ nanosheets at an infinite scan rate is 308 F/g. Thus, meaning that capacitive processes account for 308 F/g of the charge capacitance. At a scan rate of 5 mV/s, the capacitive processes account for 46% of the capacitance and at 200 mV/s, the capacitive processes account for 92% of the capacitance.

http://dx.doi.org/10.5772/62759

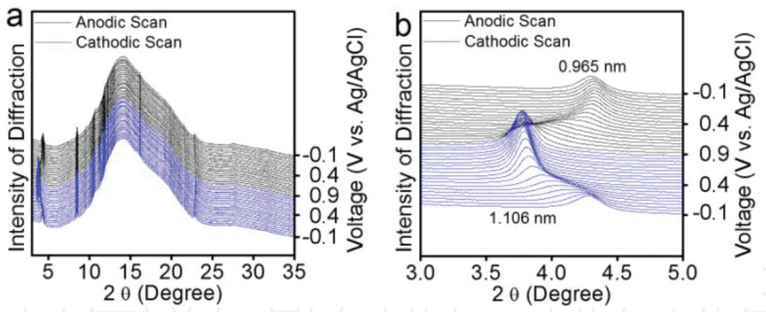


Figure 10. (a) *In situ* XRD (λ = 0.72768 Å) of the $K_{0.2}V_2O_5$ disordered nanosheets at potentials from −0.1 to 0.9 V (vs. Ag/AgCl). (b) The evolution of the (001) plane upon the CV cycling.

The intercalation of potassium ions was studied through *in situ* XRD measurement while electrochemical cycling. In **Figure 10a**, the full XRD spectra for all of the scans collected during the second cycle of the CV measurement are shown. During the anodic scan the (001), peak shifts to lower angle continuously stating an applied potential of 0.4 V all the way to 0.9 V. The d-spacing increased from 0.965 to 1.106 nm. The removal of potassium causes the oxidation of the vanadium from V^{4+} to the V^{5+} increasing the van der Waals repulsion between bilayers, which are made of the negatively charged $[VO_6]^-$ octahedra units, in turn causing the expansion in the interlayer distance.

Conversely, during the cathodic scan, the (001) peak shifts back to higher 2θ angle, decreasing the d_{001} spacing from 1.106 to 0.965 nm. The shift (001) peak during the cathodic scan is also continuously occurring between 0.4 and −0.1 V. The insertion of potassium causes the reduction of vanadium from V^{5+} to V^{4+} and causes the van der Waals repulsion between bilayers to decrease, and therefore, the d_{001} spacing decreases. The (001) peak returns to the starting 2θ angle, suggesting that the intercalation/de-intercalation of the K^+ ions are reversible in nature.

The (020) peak also shifts during cycling but at an order of magnitude smaller than that of the (001) peak. It also shifted in the opposite direction with the (001) layered peak, increasing the d_{020} upon reduction, and decreasing d_{020} upon oxidation. This shifting is caused by the increase and decrease of the V–O bond distance. The higher oxidation state of vanadium resulted in a shorter V–O bond. As with the (001) peak, the shifting in (020) appears to be completely reversible.

4. Summary

The emergence of in situ time-resolved techniques, including X-ray, neutron, and electron miscopy tools, provides us with an unprecedented opportunity to "observe," in nanoscale at millisecond time steps, the electrochemical processes in a close-to-real operation conditions. At the same time, the advent of high-performance computational tools and advance computational science methods are allowing us to analyze and predict electrochemical reactions at the nanoscale and use big data tool sets to "see" how an electrochemical reaction drives functionality under real operation conditions. In this study, we have shown the power of

combining advanced experimental, analytical, and computational tools, which help move beyond current understanding of electrochemistry and reaction engineering, in case of highly crystalline and highly disordered V_2O_5-layered nanostructure, and help leap forward into complex reaction kinetics to find new ways to convert and store energy.

Acknowledgements

This work was supported by the US Department of Energy (DOE), Office of Science, Basic Energy Sciences under Award # DE-SC0010286. Use of the National Synchrotron Light Source, Brookhaven National Laboratory, was supported by the US DOE, Office of Science, Office of Basic Energy Sciences, under Contract No. DE-AC02-98CH10886. This research used resources of the Advanced Photon Source, a US DOE Office of Science User Facility operated for the DOE Office of Science by Argonne National Laboratory under Contract No. DE-AC02-06CH11357. Research conducted at ORNL's Spallation Neutron Source was sponsored by the Scientific User Facilities Division, Office of Basic Energy Sciences, US DOE.

Author details

Daniel S. Charles and Xiaowei Teng*

*Address all correspondence to: xw.teng@unh.edu

Department of Chemical Engineering, University of New Hampshire, Durham, USA

References

[1] Hoffert MI, Caldeira K, Benford G, Criswell DR, Green C, Herzog H, et al. Advanced technology paths to global climate stability: Energy for a greenhouse planet. Science. 2002;298:981–987. doi:10.1126/science.1072357

[2] Turner JA. A realizable renewable energy future. Science. 1999;285:687–689. doi: 10.1126/science.285.5428.687

[3] Chiang YM. Building a better battery. Science. 2010;330:1485–1486. doi:10.1126/science. 1198591

[4] Palomares V, Casas-Cabanas M, Castillo-Martinez E, Han MH, Rojo T. Update on Na-based battery materials. A growing research path. Energy & Environmental Science. 2013;6:2312–2337. doi:10.1039/c3ee41031e

[5] Li Z, Young D, Xiang K, Carter WC, Chiang YM. Towards high power high energy aqueous sodium-ion batteries: The $NaTi_2(PO_4)_3/Na_{0.44}MnO_2$ system. Advanced Energy Materials. 2013;3:290–294. doi:10.1002/aenm.201200598

[6] Stevens DA, Dahn JR. High capacity anode materials for rechargeable sodium-ion batteries. Journal of the Electrochemical Society. 2000;147:1271–1273. doi: 10.1149/1.1393348

[7] Suo L, Borodin O, Gao T, Olguin M, Ho J, Fan X, et al. "Water-in-salt" electrolyte enables high-voltage aqueous lithium-ion chemistries. Science. 2015;350:938–943. doi:10.1126/science.aab1595

[8] Gleiter H. Diffusion in nanostructured metals. Physica Status Solidi B-Basic Research. 1992;172:41–51. doi:10.1002/pssb.2221720106

[9] Athouel L, Moser F, Dugas R, Crosnier O, Belanger D, Brousse T. Variation of the MnO_2 birnessite structure upon charge/discharge in an electrochemical supercapacitor electrode in aqueous Na_2SO_4 electrolyte. Journal of Physical Chemistry C. 2008;112:7270–7277. doi:10.1021/jp0773029

[10] Fukuda K, Nakai I, Ebina Y, Ma RZ, Sasaki T. Colloidal unilamellar layers of tantalum oxide with open channels. Inorganic Chemistry. 2007;46:4787–4789. doi:10.1021/ic7004002

[11] Ida S, Ogata C, Unal U, Izawa K, Inoue T, Altuntasoglu O, et al. Preparation of a blue luminescent nanosheet derived from layered perovskite $Bi_2SrTa_2O_9$. Journal of the American Chemical Society. 2007;129:8956–8957. doi:10.1021/ja073105b

[12] Kai K, Yoshida Y, Kageyama H, Saito G, Ishigaki T, Furukawa Y, et al. Room-temperature synthesis of manganese oxide monosheets. Journal of the American Chemical Society. 2008;130:15938–15943. doi:10.1021/ja804503f

[13] Liu Z, Ma R, Ebina Y, Takada K, Sasaki T. Synthesis and delamination of layered manganese oxide nanobelts. Chemistry of Materials. 2007;19:6504–6512. doi:10.1021/cm7019203

[14] Song MS, Lee KM, Lee YR, Kim IY, Kim TW, Gunjakar JL, et al. Porously assembled 2D nanosheets of alkali metal manganese oxides with highly reversible pseudocapacitance behaviors. Journal of Physical Chemistry C. 2010;114:22134–22140.

[15] Yeager M, Du WX, Si R, Su D, Marinkovic N, Teng XW. Highly efficient $K_{0.15}MnO_2$ birnessite nanosheets for stable pseudocapacitive cathodes. Journal of Physical Chemistry C. 2012;116:20173–20181. doi:10.1021/jp304809r

[16] Mas-Balleste R, Gomez-Navarro C, Gomez-Herrero J, Zamora F. 2D materials: To graphene and beyond. Nanoscale. 2011;3:20–30. doi:10.1039/C0NR00323A

[17] Tepavcevic S, Xiong H, Stamenkovic VR, Zuo XB, Balasubramanian M, Prakapenka VB, et al. Nanostructured bilayered vanadium oxide electrodes for rechargeable sodium-ion batteries. ACS Nano. 2012;6:530–538. doi:10.1021/nn203869a

[18] Yeager MP, Du WX, Bishop B, Sullivan M, Xu W, Su D, et al. Potassium-ion storage in layered $K_{0.33}V_2O_5$ electrodes for aqueous pseudocapacitors. ChemSusChem. 2013;6:2231–2235. doi:10.1002/cssc.201300480

IntechOpen

IntechOpen